Research article

Ali Rostamian*, Ehsan Madadi-Kandjani, Hamed Dalir, Volker J. Sorger and Ray T. Chen*

Towards lab-on-chip ultrasensitive ethanol detection using photonic crystal waveguide operating in the mid-infrared

https://doi.org/10.1515/nanoph-2020-0576
Received October 19, 2020; accepted March 11, 2021;
published online April 8, 2021

Abstract: Thanks to the unique molecular fingerprints in the mid-infrared spectral region, absorption spectroscopy in this regime has attracted widespread attention in recent years. Contrary to commercially available infrared spectrometers, which are limited by being bulky and cost-intensive, laboratory-on-chip infrared spectrometers can offer sensor advancements including raw sensing performance in addition to utilization such as enhanced portability. Several platforms have been proposed in the past for on-chip ethanol detection. However, selective sensing with high sensitivity at room temperature has remained a challenge. Here, we experimentally demonstrate an on-chip ethyl alcohol sensor based on a holey photonic crystal waveguide on silicon on insulator-based photonics sensing platform offering an enhanced photoabsorption thus improving sensitivity. This is achieved by designing and engineering an optical slow-light mode with a high group-index of $n_g = 73$ and a strong localization of the modal power in analyte, enabled by the photonic crystal waveguide structure. This approach includes a codesign paradigm that uniquely features an increased effective path length traversed by the guided wave through the to-be-sensed gas analyte. This PIC-based lab-on-chip sensor is exemplary, spectrally designed to operate at the center wavelength of 3.4 μm to match the peak absorbance for ethanol. However, the slow-light enhancement concept is universal offering to cover a wide design-window and spectral ranges towards sensing a plurality of gas species. Using the holey photonic crystal waveguide, we demonstrate the capability of achieving parts per billion levels of gas detection precision. High sensitivity combined with tailorable spectral range along with a compact form-factor enables a new class of portable photonic sensor platforms when integrated with quantum cascade laser and detectors.

Keywords: gas sensing; infrared; photonic crystal waveguide; spectroscopy; waveguides.

1 Introduction

Mid infrared (mid IR) absorption spectroscopy has attracted considerable attention thanks to the rovibrational signatures of compounds of interest in the solid, liquid, or gas phase in the spectral region spanning from 2 to 20 μm (500–5000 cm^{-1}) – known as the molecular fingerprint region – and orders of magnitude larger absorption cross-sections than the overtones in the near-IR [1]. One such compound, ethanol vapor (C_2H_6O), has an absorption cross-section of 2×10^{-19} cm^2/molecule at the peak absorbance of λ = 3.4 μm [2]. Monitoring the ethanol concentration is of vital importance for testing drivers' and pilots' blood alcohol content (BAC) as a measure of alcohol intoxication for medical and legal purposes and for the monitoring of chemical synthesis [3]. For precise and real-time detection of trace amounts of this gas, a compact, highly sensitive, selective, and cost-effective sensor is needed.

Conventional IR spectroscopy methods such as Fourier transform infrared (FTIR) spectroscopy [4], tunable diode laser absorption spectroscopy (TDLAS) [5], or cavity ring-down spectroscopy (CRDS) [6], to name a few, require

***Corresponding authors: Ali Rostamian**, Department of Electrical and Computer Engineering, University of Texas, 10100 Burnet Road Bldg. 160, Austin, TX 78758, USA, E-mail: ali.rostamian@utexas.edu. https://orcid.org/0000-0003-4145-284X; and **Ray T. Chen**, Department of Electrical and Computer Engineering, University of Texas, 10100 Burnet Road Bldg. 160, Austin, TX 78758, USA; and Omega Optics Inc., 8500 Shoal Creek Blvd., Bldg. 4, Suite 200, Austin, TX 78758, USA, E-mail: chenrt@austin.utexas.edu
Ehsan Madadi-Kandjani, Department of Mechanical and Aerospace Engineering, California State University, Long Beach, 1250 Bellflower Blvd. Long Beach, CA 90840, USA, E-mail: ehsan.madadi@csulb.edu. https://orcid.org/0000-0003-3216-3245
Hamed Dalir, Omega Optics Inc., 8500 Shoal Creek Blvd., Bldg. 4, Suite 200, Austin, TX 78758, USA. https://orcid.org/0000-0002-9998-3830
Volker J. Sorger, George Washington University, Washington, D.C. 20052, USA, E-mail: sorger@gwu.edu

bulky and expensive optical elements. The reason for this is because of the requirement of the gas cells to achieve an optical sufficiently-strong light–matter interaction, thus demanding large devices and hence systems. In addition, electronics to operate devices result in still benchtop systems with limited scope for portability. On the other hand, on-chip spectrometers are alignment-free and lightweight devices that, unlike their commercially available benchtop counterparts, offer sensing with a high degree of portability. This offers sensors to become an integral part in technologies with currently unattainable applications. By virtue of the slow-light effect with a high group index value and enhanced optical modal overlap with the analyte, photonic crystal waveguides (PCW) are ideal platforms for the on-chip mid IR spectroscopy [7].

Thanks to the optical transparency of up to 8 μm [8] and leveraging the already existing and mature fabrication technologies of integrated circuits, silicon is the material of choice for most passive photonic applications. Silicon-on-insulator (SOI) [9], silicon-on-sapphire (SoS) [10, 11], and free-standing silicon membranes [12, 13] can serve as platforms for mid IR optical absorption spectroscopy. SOI chips mass-produced at CMOS foundries have been widely used in the NIR applications, but the transparency window of the oxide cladding extends to 3.8 μm and can be used for mid IR applications as well [14]. Owing to the high index contrast between the silicon core and the oxide cladding, devices with small footprints can be realized on the SOI chips. Both the PC-based microcavities and PCWs have been demonstrated in free-standing silicon membranes in SOI in the mid IR wavelengths [15, 16]. Although free-standing membranes in SOI can support modes over a broader wavelength range, because of the waveguide's tendency to bend and buckle, the fabrication yield of such suspended membrane structures is low.

Enhanced optical absorbance can be achieved using a mid infrared holey PCW, as demonstrated in this work. The principle of enhanced absorption is enabled by a slow-light mode and enhanced optical field intensities in the waveguide that combine to increase the effective path length traversed by the guided wave through the sensed gas. Employing this structure, in this paper, we design and fabricate an on-chip ethyl alcohol sensor and use it to detect parts per billion (ppb) levels of ethanol vapor.

Our PCW-based gas sensors use the absorption spectroscopy scheme, which is governed by the Beer–Lambert law. According to this law, the transmitted intensity at the output of the waveguide is given by:

$$I = I_0 \exp(-\gamma \alpha_{\text{abs}} L) \tag{1}$$

Where I_0 is the incident intensity, L is the interaction length, $\alpha_{\text{abs}} = \varepsilon C$ is the absorption parameter with ε as the molar absorption and C as the concentration, and finally γ is the medium-specific absorption factor and is determined by dispersion-enhanced light–matter interaction, and is given by: $\gamma = f \times (c/n)/v_g$ [17]. Where c is the velocity of light in free space, v_g is the group velocity in the medium of effective index n, and f is the fill factor also known as mode overlap factor denoting the relative fraction of the optical field residing in the analyte medium. A photonic crystal waveguide can enhance light–matter interaction through engineering both the group index and the filling factor, as discussed next.

2 Device description

Figure 1(a) shows a schematic illustration of the sensor structure and its working principle. The holey PCW comprises of a hexagonal lattice of air holes within a slab of silicon with a single missing row of holes along the Γ–K direction. The air holes in the bulk have a radius of $r = 0.22a$, where a is the lattice constant, and the missing row in the center of PCW is replaced with smaller holes with radius r_s. The waveguide is a W1 line defect meaning the width of the waveguide is $1 \times \sqrt{3}a$. Using plane-wave expansion method, the structure was optimized and designed to ensure a relatively large guiding bandwidth for the PCW-guided mode as well as a wide stopgap. A relatively wide stopgap will ensure a more accurate demarcation of the bandedge and slow-light guiding region.

The BandSolve package of the Rsoft is used to calculate the dispersion diagram of the photonic crystal and 3D electric field intensity profile of the propagating light. Figure 1 shows the simulation results performed using the three-dimensional plane-wave expansion method. The dispersion diagram of the photonic crystal is depicted in Figure 1(b), where the red curve corresponds to the defect-guided mode, and the black dashed line indicates the oxide light line. As observed, the defect-guided PC mode can propagate below the oxide light-line without any overlap with modes above the light line. Figure 1(c) plots the guided mode bandwidth below the oxide light line and the stopgap region width in terms of normalized frequency (a/λ) versus the ratio of the radius of the small air holes to the radius of bulk air holes (r_s/r). Here, the design constraint is to ensure the coexistence of a relatively large guiding bandwidth for the propagating slow-light mode and a wide stopgap. Accordingly, for the optimized device, highlighted by the red dashed circle in Figure 1(c), an optimal relative small hole radius of $r_s = 0.7r$ is chosen. Figure 1(d) illustrates the 3D electric field intensity

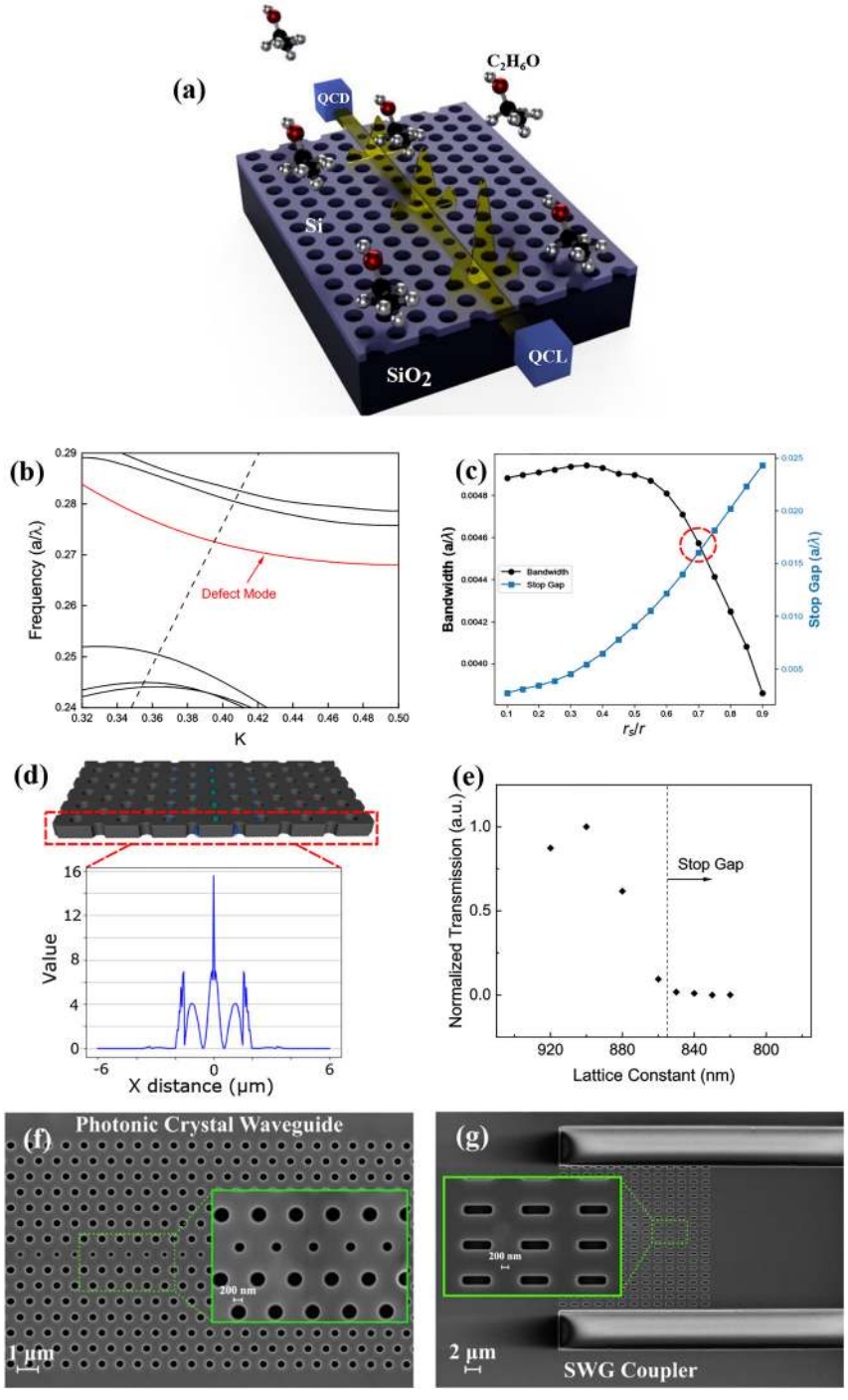

Figure 1: (a) Schematic illustration of the sensor and its working principle. The holey photonic crystal waveguide is a W1 line defect formed by etching a row of smaller air holes in the center of the hexagonal photonic crystal. (b) Dispersion diagram of the photonic crystal simulated by 3D plane-wave expansion, defect-guided mode denoted by red solid line, black dashed line indicates the oxide light-line. (c) Variations of the photonic crystal bandwidth and stopgap in terms of normalized frequency (α/λ) as a function of the relative radius (r_s/r). (d) 3D electric field intensity profile of the propagating light in the waveguide. Inset depicts the cross-section of the electric field intensity profile at the position as shown by red dash line. (e) Measured transmitted intensity through PCW devices with different lattice constants to demarcate stop gap boundary. (f) Top-view SEM image of the photonic crystal waveguide (g) Top-view SEM image of the TE polarization selective subwavelength grating coupler, scale bar for insets is 200 nm.

profile of the propagating light in the waveguide. Inset depicts the cross-section of the electric field intensity profile at the position as shown by red dash line. The results show a factor of 15 enhancements in the electric field intensity in the center of the holey PCW compared to the strip waveguide, indicating a strong optical localization at the defect holes where interaction between the optical mode and the analyte is strongest.

The PCW devices are fabricated on an SOI wafer with a 500 nm thick silicon layer over a 3 μm thick buried oxide (BOX) layer, and the pattern of the passive waveguides is transferred to the silicon device layer using electron beam lithography and inductively coupled plasma etching. A 200 nm silicon dioxide layer is first deposited on top of the silicon layer using plasma-enhanced chemical vapor deposition to serve as a hard mask for pattern transfer. All

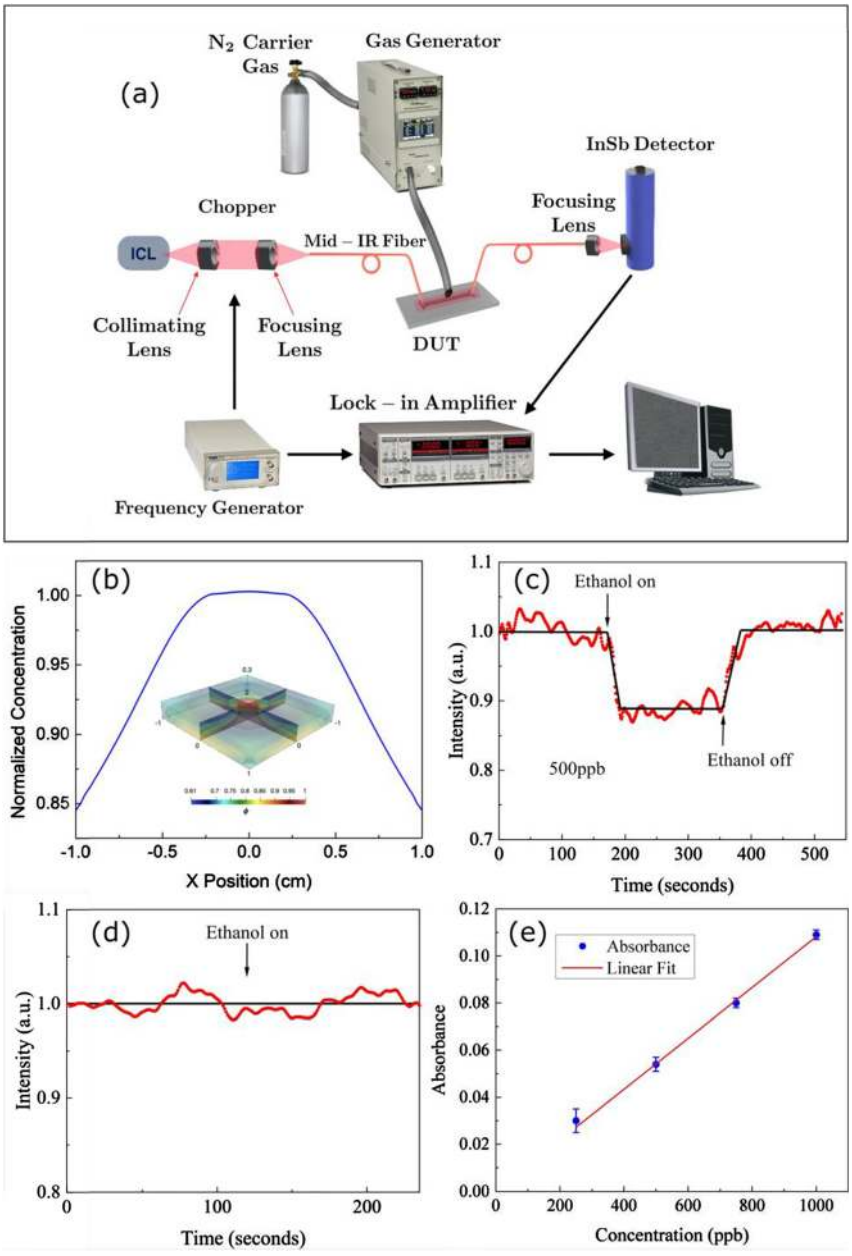

Figure 2: (a) Schematic representation of the measurement setup for gas sensing. (b) Gas concentration along the X axis at $y = 0$ and $z = 0$, inset is the steady-state gas concentration distribution over the sample normalized to the concentration delivered by the vapor generator. (c) Measured transmitted light intensity through the 9 mm long PCW when exposed to 500 ppb of ethanol vapor. (d) Measured transmitted light intensity through the 1 cm long strip waveguide when exposed to 5 ppm of ethanol vapor. (e) Sensing data for a 9 mm long PCW exposed to different concentrations of ethanol, red solid line is the best linear fit of the data.

the components are patterned in one step using the JEOL JBX-6000FS electron-beam lithography tool with ZEP-520A e-beam resist, followed by developing in n-Amyl acetate (ZEP-N50) for 2 min, and rinsing in isopropyl alcohol. The e-beam resist pattern is next transferred to silicon dioxide by reactive ion etching using CHF_3 and O_2 at 400 V DC bias and 40 mTorr. Following this, the pattern in silicon dioxide is transferred to silicon by inductively coupled plasma (ICP) etch using HBr and Cl_2 at 400 W ICP power, 200 W RF power, 10 mTorr pressure, and 20 Torr helium flow for backside cooling. Finally, the chip is cleaned using piranha, followed by three cycles of piranha/HF postprocess treatment.

Figure 1(f) and 1(g) show the top-view SEM image of the photonic crystal waveguide and TE polarization selective subwavelength grating couplers. As in previous research [18–20], a photonic crystal index taper is inserted at both interfaces of the PCW and strip waveguides. By providing optical impedance matching, this taper reduces Fresnel reflection losses that would otherwise lead to significant fringe patterns in the PCW guided mode transmission spectrum. Since the single-mode fibers are not polarization maintaining the input and output grating couplers are also designed and implemented to couple the light into and out of the waveguides.

3 Results and discussion

Figure 2(a) illustrates a schematic representation of the measurement setup employed for gas sensing. The light emitted from a single wavelength interband cascade laser is collimated and coupled into a single-mode chalcogenide fiber with aspheric and biconvex lenses, respectively. Input light coupled in from the fiber via the grating couplers propagates through the photonic crystal waveguides, and the transmitted light is coupled out of the waveguide through output gratings. A Calibrated concentration of ethanol diluted in nitrogen is flowed from a commercial Kin–Tek vapor generator to the chip. Finally, the output signal is collected by a multimode chalcogenide fiber and measured by an InSb detector connected to a lock-in amplifier that demodulates the signal that was chopped by a mechanical chopper earlier to enhance signal-to-noise ratio.

Numerical simulation is performed to study gas distribution on the surface of the chip under the tubing outlet. The sample was modeled assuming a rectangular computational domain whose width is 2 cm in x and y direction, and the gas is flowed over the chip using a circular pipe. This domain was discretized into a total of 279,000 hexahedral computational cells. The flow field was simulated using the steady-state incompressible solver in OpenFOAM and the k–ε turbulence model, which is provided by OpenFOAM. Convection terms for all the conservation equations were discretized with a limited second-order central scheme. Once the converged flow field was obtained the solution of the gas concentration was started, assuming the flow field was frozen.

The concentration of the gas on top of the sensor is found by using the transport equation for the passive scalar, using the pre specified stationary velocity field. The convection–diffusion scalar transport equation without source terms solves the concentration dispersion inside the sensor domain.

$$\frac{d\phi}{dt} + \nabla \cdot (U\phi) - \nabla^2 (D_T \phi) = 0 \tag{2}$$

Where ϕ is the transported scalar, U is the fluid velocity, and D_T is the diffusion coefficient divided by the fluid density. The initial concentration of the gas at the inlet is assumed to be normalized and set to 1. Figure 2(b) shows the calculated normalized concentration of gas over the sample when 250 ppm of ethanol vapor is coming out of the tubing outlet. Simulation results indicate that depending on the length of the photonic crystal, the gas concentration on the surface of the waveguide under the tubing outlet is slightly lower than the gas concentration delivered by the vapor generator. So, for each device, the concentration of the generator is adjusted to compensate for the difference.

Our devices are characterized using a single wavelength external source with a center wavelength of λ = 3.4 μm. So, to demarcate the stopgap and light line boundaries, similar devices with different lattice constants but a constant r/a ratio were fabricated and measured. Figure 1(e) plots the normalized transmitted intensity through the PCW devices with varying lattice constants. As observed, the devices with lattice constants less than 850 nm had practically zero output power since they fall within the stopgap, and the photonic crystals waveguides with a greater than 850 nm are above the stopgap band edge. The sensitivity of the device is a strong function of the position of the band edge and hence fabrication process. The photonic crystal waveguide with a lattice constant of a = 860 nm was chosen for sensing. The group index is inversely proportional to the group velocity in Equation (1). The estimated group index value extracted from the dispersion diagram of the guided mode that propagates through the waveguide at λ = 3.4 μm is $n_g \sim 73$ compared to a refractive index of n = 1 in air. As detailed in the Supplementary Material, this mode's index is ~18.8 times larger than the group index of the fundamental TE mode in the strip waveguide. Figure 1(d) also shows a factor of 15 enhancements in the electric field intensity compared to the strip waveguide in the center of the holey PCW. As described in the Supplementary Material, based on the FDE mode calculation the optical overlap integral (f) for the fundamental TE in strip waveguide is ~2.5%, whereas the high n_g propagating mode in the photonic crystal waveguide has an overlap factor of ~17.1%. The effective absorption is enhanced as a result of a slow group velocity combined with a large electric field overlap with the analyte. These 2D photonic crystal waveguide structures are inherently narrowband, as is evident in the dispersion diagram of the PCW in Figure 1(b), which further guarantees the selective detection of the gas species of interest at the peak absorbance wavelength.

Figure 2(c) illustrates a gas sensing measurement data. It shows the normalized transmitted light intensity through a 9 mm long holey photonic crystal waveguide when exposed to 500 ppb of ethanol gas plotted as a function of time. Ethanol was flowed from a calibrated Kin–Tek vapor generator in a nitrogen carrier gas. The carrier gas is always ON. An 11.7% drop in the transmitted signal through the photonic crystal waveguide is observed when ethanol flow is turned ON. When ethanol flow is turned OFF, the signal goes back to the original levels in nitrogen flow. As shown

in Figure 2(d), when the PCW waveguide is replaced with a 1 cm long strip waveguide and exposed to a much higher ethanol concentration of 5 ppm, no drop in the transmitted signal is observed.

Figure 2(e) plots the sensing data for a 9 mm long PCW when exposed to different concentrations of ethanol. Absorbance values are calculated from transmission data measured in the presence of different gas concentrations. The solid red line is the best linear fit of the data. The black dashed line is an extrapolation of the data points, and the error bars denote the standard error of the multiple measurements. There are various sources of noise, including mechanical noises originating from vibrations, light source fluctuations, and the noise associated with the InSb detector. A smaller limit of detection is easily feasible by eliminating these background noises.

The vapor generator could provide concentrations of down to 250 ppb. The standard deviation for the blank measurement is 0.03. Thereby, the limit of detection (LOD) for this device calculated by three times the standard deviation, 3σ, and the slope of the curve in Figure 2(e) would be 138 ppb. Table1 summarizes the performance comparison of different ethanol sensors. In another study, L. Tombez et al. have also demonstrated a methane absorption sensor using a silicon strip waveguide with a paperclip geometry with the capability of achieving down to 10 ppm gas detection precision [26]. It is evident that our proposed sensor excels the others in detection limit. This sensor can be deployed to unambiguously detect the molecular composition of a wide variety of gases, liquids, or solids in a non intrusive way.

Regarding portability, formfactor improvements the entire sensing platform can be further miniaturized using photonic integration and emerging concepts offering light–matter interaction enhancements and electro-optic control; for instance, ensuring a sufficiently high signal to noise ratio, but not relying on a bulky chopper and log-in amplifier, both could be replaced, for instance, with electro optic modulators and CMOS circuitry, respectively. For example, while silicon photonics offers millimeter modulators, we recently demonstrated plasmonic-based <5 μm compact V_π phase shifters [27] and a photonic MZI modulators [28] both in Silicon PICs for allowing modulating ('chopping') light from the laser source. The added benefits from a modulator over mechanical choppers are more data can be samples per unit time window. As an efficient and formfactor-benign detection platform, waveguide-integrated schemes can be deployed in combination with emerging materials options, such as thin two-dimensional (2D) semiconductor materials [29] that, unlike compound semiconductors relying on epitaxy, do not require any substrate lattice matching. In fact, these 2D quantum well can be cross-contamination-free transferred anywhere on the PIC with sub micrometer alignment precision within seconds [30]. In regard to enhancing the detector efficiency, SOI rip waveguides can be augmented with metallic slot designs which allow for not only increasing the mode overlap with heterogeneously-added materials atop the silicon waveguide ACS [31], but also enable for new design paradigms enabling high gain-bandwidth-product detectors that are not limited by the transport (transit time) originating from a low mobility [32]. Also, concepts of strainoptronics can be used as a new degree of design freedom on PICs, for instance, to tailor and tune the absorption region of a sensors cavity or back-end detector [33]. Lastly, with the wavelength were most gas species show resonance absorption lines being in the mid IR spectral region, the light-source would be ideally a THz sources, such as offered by a quantum cascade laser [34]. Such THz and mid IR light generation concepts could again be combined with nanophotonic scaling law concepts such as high Purcell-factors enabling high pump efficiency via mode selection [35], or with emerging material PIC-integration [36–38].

The generalized nature of this versatile sensing platform will enable applications beyond ethanol sensing and breath alcohol monitoring to include the monitoring of cancers and infectious diseases and in industrial air quality monitoring on airborne platforms, and in law-enforcement and fire-fighting applications.

Table 1: Performance comparison of ethanol sensors.

Sensor	Working principle	Detection limit	Response time	Reference
Functionalized CNT	Electrochemical	3ppm	2 min	[21]
Tapered optical fiber	Optical (evanescent field)	140 ppm	5 s	[22]
Porous microrods	Resistive	10 ppm	10 s	[23]
TiO_2/Pt nanostructure	Optical (UV irradiation)	10 ppm	380 s	[24]
Capacitive nanoporous film	Capacitive	130 ppm	5–10 min	[25]
2D PCW	Optical (enhanced optical field, slow-light effect)	250 ppb	20–30 s	Present work

4 Summary

In summary, we experimentally demonstrate an ethyl alcohol sensor based on a holey photonic crystal waveguide concept offering an optical slow light mode yet chemical accessibility on a silicon on insulator platform. This approach allows for a high-degree of spectral tunability, thus allowing designs with high chemical selectivity via overlaying the waveguide's spectral high group index (slow light) region with that of gas specimen, exemplary demonstrating 3.4 μm resonances for the peak absorbance of ethanol. This approach enables a sensing sensitivity of achieving ten's of parts per billion gas detection precision, just limited by the mechanical noises originating from vibrations and light source fluctuations. Beyond ethanol, this sensing concept is not limited to the demonstrated absorption, but readily scalable to other wavelengths enabling the detection of a number of gas species. Furthermore, this slow light-based enabled photonic lab-on-chip sensing platform can be further integrated deploying a number of recent nanophotonic concepts and light–matter interaction enhancement techniques as well as heterogeneous integration of emerging materials into silicon photonics platform to include quantum cascade light source and detection, strainoptronics, and Van der Waals semiconductor quantum wells.

Author contributions: All the authors have accepted responsibility for the entire content of this submitted manuscript and approved submission.
Research funding: The authors appreciate the significant contribution of Dr. S. Chakravarty. The research was supported in part by the NIH Grant # 1 R43 AA026122-01 and in part by the National Science Foundation (NSF) under Contract 1932753. The authors also acknowledge the use of Texas Nanofabrication Facilities supported by the NSF NNCI Award #1542159.
Conflict of interest statement: The authors declare that they have no conflict of interest.

References

[1] X. Xu, C.-J. Chung, S. Chakravarty, R. T. Chen, and Y. Zou, "Mid-infrared silicon photonic waveguides and devices [Invited]," *Photonics Res.*, vol. 6, no. 4, p. 254, 2018.
[2] G. C. Rhoderick, P. M. Chu, P. A. Johnson, R. L. Sams, S. W. Sharpe, and T. J. Johnson, "Gas-phase databases for quantitative infrared spectroscopy," *Appl. Spectrosc.*, vol. 58, no. 12, pp. 1452–1461, 2004.
[3] I. V. Anoshkin, A. G. Nasibulin, P. R. Mudimela, M. He, V. Ermolov, and E. I. Kauppinen, "Single-walled carbon nanotube networks for ethanol vapor sensing applications," *Nano Res.*, vol. 6, no. 2, pp. 77–86, 2013.
[4] C. Berthomieu and R. Hienerwadel, "Fourier transform infrared (FTIR) spectroscopy," *Photosynth. Res.*, vol. 101, no. 2–3, pp. 157–170, 2009.
[5] M. Lackner, "Tunable diode laser absorption spectroscopy (TOLAS) in the process industries-a review," *Revi. Chem. Eng.*, vol. 23, no. 2, pp. 65–147, 2007.
[6] M. J. Thorpe, K. D. Moll, R. J. Jones, B. Safdi, and J. Ye, "Broadband cavity ringdown spectroscopy for sensitive and rapid molecular detection," *Science*, vol. 311, no. 5767, pp. 1595–1599, 2006.
[7] T. Hemati and B. Weng, "The mid-infrared photonic crystals for gas sensing applications," in *Photonic Crystals - A Glimpse of the Current Research Trends [Working Title]*, IntechOpen, 2019. Available at: https://doi.org/10.5772/intechopen.80042.
[8] R. Soref, "Mid-infrared photonics in silicon and germanium," *Nat. Photonics*, vol. 4, no. 8, pp. 495–497, 2010.
[9] J. S. Penadés, C. Alonso-Ramos, A. Z. Khokhar, et al., "Suspended SOI waveguide with sub-wavelength grating cladding for mid-infrared," *Opt. Lett.*, vol. 39, no. 19, p. 5661, 2014.
[10] A. Rostamian, J. Guo, S. Chakravarty, et al., "Grating-coupled silicon-on-sapphire polarization rotator operating at mid-infrared wavelengths," *IEEE Photonics Technol. Lett.*, vol. 31, no. 5, pp. 401–404, 2019.
[11] A. Rostamian, J. Guo, S. Chakravarty, C. J. Chung, D. Nguyen, and R. T. Chen, "Parts-per-billion carbon monoxide sensing in silicon-on-sapphire mid-infrared photonic crystal waveguides," in *Conference on Lasers and Electro-Optics, San Jose, CA*, IEEE, 2018, p. ATh1O.4.
[12] J. Chiles, S. Khan, J. Ma, and S. Fathpour, "High-contrast, all-silicon waveguiding platform for ultra-broadband mid-infrared photonics," *Appl. Phys. Lett.*, vol. 103, no. 15, p. 151106, 2013.
[13] A. Sánchez-Postigo, G. Wangüemert-Pérez, J. S. Penadés, et al., "Suspended silicon integrated platform for the long-wavelength mid-infrared band," in *International Conference on Transparent Optical Networks, Angers, France*, vol. 2019-July, IEEE, 2019.
[14] S. A. Miller, M. Yu, X. Ji, et al., "Low-loss silicon platform for broadband mid-infrared photonics," *Optica*, vol. 4, no. 7, p. 707, 2017.
[15] R. Shankar, R. Leijssen, I. Bulu, and M. Lončar, "Mid-infrared photonic crystal cavities in silicon," *Opt. Express*, vol. 19, no. 6, p. 5579, 2011.
[16] C. Reimer, M. Nedeljkovic, D. J. M. Stothard, G. Z. Mashanovich, and T. F. Krauss, "Mid-infrared photonic crystal waveguides in SOI," in *IEEE International Conference on Group IV Photonics GFP,* San Diego, CA, USA, vol. 20, no. 28, IEEE, 2012, pp. 12–14.
[17] N. A. Mortensen and S. Xiao, "Slow-light enhancement of Beer-Lambert-Bouguer absorption," *Appl. Phys. Lett.*, vol. 90, no. 14, p. 141108, 2007.
[18] Y. Zou, S. Chakravarty, L. Zhu, and R. T. Chen, "The role of group index engineering in series-connected photonic crystal microcavities for high density sensor microarrays," *Appl. Phys. Lett.*, vol. 104, no. 14, p. 141103, 2014.
[19] Y. Zou, S. Chakravarty, P. Wray, and R. T. Chen, "Mid-infrared holey and slotted photonic crystal waveguides in silicon-on-

sapphire for chemical warfare simulant detection," *Sensor. Actuator. B Chem.*, vol. 221, pp. 1094–1103, 2015.
[20] W. C. Lai, S. Chakravarty, X. Wang, C. Lin, and R. T. Chen, "Photonic crystal slot waveguide absorption spectrometer for on-chip near-infrared spectroscopy of xylene in water," *Appl. Phys. Lett.*, vol. 98, no. 2, p. 023304, 2011.
[21] Q. Nie, W. Zhang, L. Wang, et al., "Sensitivity enhanced, stability improved ethanol gas sensor based on multi-wall carbon nanotubes functionalized with Pt-Pd nanoparticles," *Sensor. Actuator. B Chem.*, vol. 270, pp. 140–148, 2018.
[22] W. Liu, Y. Hu, and Y. Hou, "Ethanol gas sensitivity sensor based on roughened POF taper of modified polypyrrole films," *Sensors*, vol. 20, no. 4, p. 989, 2020.
[23] J. Tan, J. Chen, K. Liu, and X. Huang, "Synthesis of porous α-Fe2O3 microrods via in situ decomposition of FeC2O4 precursor for ultra-fast responding and recovering ethanol gas sensor," *Sensor. Actuator. B Chem.*, vol. 230, pp. 46–53, 2016.
[24] R. Maolanon, W. Wongwiriyapan, and S. Pratontep, "TiO2/Pt/TiO2 sandwich nanostructures: towards alcohol sensing and UV irradiation-assisted recovery," *J. Chem.*, vol. 2017, 2017, https://doi.org/10.1155/2017/8545690.
[25] M. S. Hosseini, S. Zeinali, and M. H. Sheikhi, "Fabrication of capacitive sensor based on Cu-BTC (MOF-199) nanoporous film for detection of ethanol and methanol vapors," *Sensor. Actuator. B Chem.*, vol. 230, pp. 9–16, 2016.
[26] L. Tombez, E. J. Zhang, J. S. Orcutt, S. Kamlapurkar, and W. M. J. Green, "Methane absorption spectroscopy on a silicon photonic chip," *Optica*, vol. 4, no. 11, p. 1322, 2017.
[27] R. Amin, R. Maiti, Y. Gui, et al., "Sub-wavelength GHz-fast broadband ITO Mach–Zehnder modulator on silicon photonics," *Optica*, vol. 7, no. 4, p. 333, 2020.
[28] R. Amin, R. Maiti, C. Carfano, et al., "0.52 v mm ITO-based Mach-Zehnder modulator in silicon photonics," *APL Photonics*, vol. 3, no. 12, p. 126104, 2018.
[29] R. Maiti, R. A. Hemnani, R. Amin, et al., "A semi-empirical integrated microring cavity approach for 2D material optical index identification at 1.55 μm," *Nanophotonics*, vol. 8, no. 3, pp. 435–441, 2019.
[30] R. A. Hemnani, J. P. Tischler, C. Carfano, et al., "2D material printer: A deterministic cross contamination-free transfer method for atomically layered materials," *2D Mater.*, vol. 6, no. 1, p. 015006, 2019.
[31] Z. Ma, K. Kikunaga, H. Wang, et al., "Compact graphene plasmonic slot photodetector on silicon-on-insulator with high responsivity," *ACS Photonics*, vol. 7, no. 4, pp. 932–940, 2020.
[32] V. J. Sorger and R. Maiti, "Roadmap for gain-bandwidth-product enhanced photodetectors: opinion," *Opt. Mater. Express*, vol. 10, no. 9, p. 2192, 2020.
[33] R. Maiti, C. Patil, M. A. S. R. Saadi, et al., "Strain-engineered high-responsivity MoTe2 photodetector for silicon photonic integrated circuits," *Nat. Photonics*, vol. 14, no. 9, pp. 578–584, 2020.
[34] B. S. Williams, "Terahertz quantum cascade lasers," in *Asia Optical Fiber Communication and Optoelectronic Exposition and Conference, Shanghai China*, Optical Society of America (OSA), 2008, p. SuG3.
[35] K. Liu, S. Sun, A. Majumdar, and V. J. Sorger, "Fundamental scaling laws in nanophotonics," *Sci. Rep.*, vol. 6, no. 1, pp. 1–12, 2016.
[36] K. Liu and V. J. Sorger, "Electrically-driven carbon nanotube-based plasmonic laser on silicon," *Opt. Mater. Express*, vol. 5, no. 9, p. 1910, 2015.
[37] R. F. Oulton, V. J. Sorger, T. Zentgraf, et al., "Plasmon lasers at deep subwavelength scale," *Nature*, vol. 461, no. 7264, pp. 629–632, 2009.
[38] K. Liu, N. Li, D. K. Sadana, and V. J. Sorger, "Integrated nanocavity plasmon light sources for on-chip optical interconnects," *ACS Photonics*, vol. 3, no. 2, pp. 233–242, 2016.

Supplementary Material: The online version of this article offers supplementary material (https://doi.org/10.1515/nanoph-2020-0576).